Photodegradation of Phenol under Visible Light Irradiation Using Cu-N-codoped ZrTiO₄ Composite as a High-Performance Photocatalyst

Wanda Putra Fauzi[1], Rian Kurniawan[2], Sri Sudiono[1], Niko Prasetyo[1], and Akhmad Syoufian[1*]

[1]*Department of Chemistry, Faculty of Mathematics and Natural Sciences, Universitas Gadjah Mada, Sekip Utara, Yogyakarta 55281, Indonesia*

[2]*Institute of Chemical Technology, Universität Leipzig, Linnéstr. 3, Leipzig 04103, Germany*

Abstract: *Codoping of nitrogen and copper into zirconium titanate composite (Cu-N-codoped ZrTiO₄) was carried out through a sol-gel process. This study aimed to investigate the effect of copper and nitrogen dopants on the photocatalytic activity of ZrTiO₄ composite in degrading phenol. To prepare the composite, an aqueous suspension of zirconia (ZrO₂) alongside a fixed amount of urea and various amount of copper sulfate was added dropwise into diluted titanium(IV) tetraisopropoxide (TTIP) in ethanol. The composites were calcined at temperatures of 500, 700, and 900 °C. Fourier-transform infrared spectrophotometry (FTIR), X-ray diffraction (XRD), scanning electron microscopy with energy dispersive X-ray (SEM-EDX) mapping, and specular reflectance UV-visible spectrophotometry (SR UV-vis) were used for their characterization of composite. The photocatalytic activity was evaluated by adding the composite into a 10 mg L⁻¹ phenol solution for various irradiation time spans. The remaining concentration of phenol solution was determined by absorption at 269 nm. Cu-N-codoped ZrTiO₄ composite containing 5% Cu calcined at 500 °C demonstrated the highest observed rate constant and a significant band gap decrease from 3.13 to 2.68 eV.*

Keywords: *band gap; Cu-N-codoped ZrTiO₄; degradation; phenol*

■ INTRODUCTION

The problem of water scarcity has been increasing around the world. Wastewater recycling has become an urgent solution to this problem [1]. Phenol is one of the most dangerous pollutants in wastewater because of its high toxicity and carcinogenicity, even at low concentrations. Phenols are regularly used in petrochemicals, pharmaceuticals, oil refining, pulp, paper, and wood manufacturing processes [2-4]. Numerous ways of decomposing wastewater have been established, including adsorption and biodegradation in industrial processes. However, those methods have some downsides, including high operational costs and the use of toxic chemical reagents [5-6]. The removal of phenol pollutants has become a key requirement in tackling environmental problems, and photocatalytic systems have been extensively researched for the removal of

contaminants [7]. In the photocatalytic process, light energy is required for the excitation of the photocatalyst to generate charged carriers for the degradation process [8]. Electrons or holes initiate the process of radical species formation in the form of superoxide radicals (•O²⁻). The •O²⁻ reacts with water to produce hydroxyl ions (OH⁻). The OH⁻ then reacts with holes (h+) to form hydroxyl radicals (•OH). These •OH break down phenol compounds into simpler molecules, such as CO_2 and H_2O [9-10]. The photocatalyst material is a metal oxide semiconductor with a corresponding band gap energy of about 1.7–3.2 eV [11].

Titanium dioxide or titania (TiO_2), a metal oxide semiconductor, has received considerable research attention as a photocatalyst. Numerous photocatalyst systems have been explored, but TiO_2 stands out due to its unique properties. TiO_2 possesses a relatively high oxidation/reduction potential, strong chemical stability,

520

Indones. J. Chem., 2024, 24 (2), 519 - 529

photo-corrosion resistance, inexpensive cost, and non-toxicity. The anatase phase of TiO$_2$ has a band gap of 3.2 eV and an activity in the ultraviolet (UV) range of λ less than 385 nm [7,12]. TiO$_2$ exists in three phases: rutile, anatase, and brookite. Rutile is the most stable phase of TiO$_2$, while anatase is metastable. Brookite transforms to rutile at temperatures above 600 °C [13]. The energy gap of the anatase phase of TiO$_2$ is slightly higher (3.20 eV) than that of the rutile phase (3.02 eV). However, the anatase phase gives better photoactivity under UV irradiation [14].

In addition, zirconia (ZrO$_2$) possesses low thermal conductivity, corrosion resistance, and excellent mechanical and photothermal properties. The wide band gap of ZrO$_2$ (approximately 5 eV) results in particularly strong photogenerated redox performance under UV irradiation [15]. Due to its wide band gap, ZrO$_2$ is inefficient under solar radiation [16]. ZrO$_2$ has high stability and readily generates holes in its valence band, resulting in strong interactions with the active component. ZrO$_2$ exists in three polymorphic phases: monoclinic (< 1170 °C), tetragonal (1170–2370 °C), and cubic (> 2370 °C) [17]. ZrO$_2$ is only active in the UV range, and hence, modification is necessary to increase its photocatalytic performance. Among these, an effective way to enhance the photocatalytic activity of ZrO$_2$ is to combine ZrO$_2$ with a TiO$_2$ semiconductor. Studies predict that the incorporation of ZrO$_2$ into TiO$_2$ increases the stability of anatase compared to rutile [18].

A composite of ZrO$_2$ coupled with TiO$_2$ (ZrO$_2$-TiO$_2$, ZrTiO$_4$) can generate a higher photocatalytic activity than pure TiO$_2$, has a smaller band gap than pure ZrO$_2$, and shows good thermal stability [19]. This coupling will offer the added benefits of large surface area, high thermal stability, and corrosion resistance [20]. Doping of ZrTiO$_4$ with metals, such as Fe [21], Mn [22], and Zn [23], as well as non-metals such as N [24] and C [25], has been reported to decrease the band gap to visible light. Copper (Cu) and nitrogen (N) have been chosen as the dopants for this work, as they both have excellent efficiency in separating the charge carriers. Several intrinsic properties of metal oxide ions, such as mechanical properties and conductivity, are enhanced by nitrogen doping [26].

Codoping methods of Cu and N into ZrTiO$_4$ composite have been reported, such as the template-free hydrothermal [27] and the polymer complex solution process [28]. Both methods still employ toxic organic solvents, which are also expensive and can pollute the environment. The sol-gel method ensures the homogeneous mixing of components at the molecular level, hence facilitating the incorporation process of dopants into the material matrix. Ti–O–Zr bonding was observed by Rahmawati et al. [29] on a Cu-N-ZrTiO$_4$ composite prepared using the sol-gel method. The gel has a denser concentration of oxygen vacancies, which enhances the photocatalytic activity for the removal of phenol [30]. Kambur et al. [31] have reported that almost 100% removal of phenol by ZrO$_2$-TiO$_2$ composite under UV lamp illumination for 90 min.

In this study, ZrTiO$_4$ material was doped with Cu and N together by the sol-gel method. Urea and copper sulfate were used as nitrogen and copper sources, respectively. The effect of Cu doping on the band gap shift of nitrogen-doped ZrTiO$_4$ was investigated using different amounts of copper doping (1, 3, 5, 7 and 9% w/w with respect to titanium). The crystal structure of the photocatalyst material was studied by varying the calcination temperatures (500, 700, and 900 °C). Then, the Cu-N-doped ZrTiO$_4$ composite was applied to the degradation of phenol under visible light irradiation.

■ EXPERIMENTAL SECTION

Materials

Titanium(IV) tetraisopropoxide (TTIP) in 97% purity from Sigma-Aldrich was used as a precursor, while ZrO$_2$ (powder) from Jiaozuo Huasu was used as the coupling metal oxide. Copper(II) sulfate pentahydrate (CuSO$_4$·5H$_2$O) and urea, both from Merck, were used as dopant sources. Absolute ethanol with 98% purity from Merck and demineralized water from Jaya Sentosa were used as solvents. Phenol (Merck) was used as a target compound for photodegradation.

Instrumentation

Functional groups of the composite were determined by using Fourier-transform infrared (FTIR)

Thermo Nicolet iS10 in the range of 400 to 4000 cm^{-1}. X-ray diffractometer (XRD) PANalytical X'Pert PRO MRD was employed to determine the crystal structure under the measurement conditions of Cu Kα radiation with a wavelength of 1.54 Å, a voltage of 40 kV, and a current of 30 mA. Scanning electron microscope energy dispersive X-ray spectrometer (SEM-EDX) JSM-6510LA series with an accelerating voltage of 2000 kV was used to probe the morphology and localized copper-nitrogen dopant content on the photocatalyst surface.

Specular reflectance UV-vis spectrometer UV 1700 Pharmaspec (SR UV-vis) was utilized to measure the absorption of composites and estimate the band gap. The photocatalytic activity was evaluated under the illumination of a LIFE MAX 30W/765 PHILIPS TLD lamp. Thermo Scientific Genesys 50 UV-vis spectrophotometer (Antylia Scientific, US) was used to determine the concentration of phenol after degradation at 269 nm of maximum phenol wavelength.

Procedure

Synthesis of Cu-N-codoped ZrTiO$_4$

Cu-N-codoped ZrTiO$_4$ materials were prepared through a sol-gel process and the Cu concentration was varied with the ratio of 1, 3, 5, 7, and 9% (w/w to Ti). Firstly, 2.5 mL of TTIP was homogeneously dissolved in 25.0 mL of absolute ethanol. In a separate glass beaker, 1.0 g of ZrO$_2$ powder and 86.8 mg of urea (10% w/w to Ti) were dispersed in 10.0 mL of demineralized water along with CuSO$_4$·5H$_2$O. The aqueous suspension was then added dropwise and followed by stirring for 30 min. The suspension was centrifuged at 2,000 rpm for 1 h, and the resulting precipitate was left to dry by air for 24 h. The composite solid was then dried at 80 °C for 24 h and calcined at 500, 700, and 900 °C for 4 h under atmospheric conditions.

The composites were labelled as αCu-N-ZT-β, in which α is the percentage of Cu dopant and β is the calcination temperature in °C. All composites were characterized using FTIR, XRD, SEM-EDX mapping, and SR UV-vis. The crystal size (L) is calculated by the Scherrer equation (Eq. (1)) [19];

$$L = \frac{0.9\lambda}{B\cos\theta} \tag{1}$$

where λ is the wavelength of the X-ray in nm, θ is the Bragg angle, and B is half the full width of the maximum intensity of the peak in radians.

Photocatalytic degradation of phenol

Cu-N-codoped ZrTiO$_4$ with various concentrations of Cu dopant (100 mg) was dispersed in 100 mL of 10 mg L^{-1} aqueous phenol (Ph). The mixture was stirred for 15 min before irradiation to allow for Ph adsorption on the photocatalyst. The mixture was then continuously stirred and irradiated for 15, 30, 45, 60, 75, 90, 105, and 120 min using a LIFE MAX 30W/765 PHILIPS TLD lamp. The photocatalyst was separated by centrifugation at 3,000 rpm for 30 min. The concentration of Ph after photocatalytic degradation was determined by absorption at 269 nm. The qualitative analysis for photodegradation is calculated using the pseudo-first-order Langmuir-Hinshelwood kinetic model, which is given by Eq. (2) [32];

$$r = \frac{k_r K_L C}{1 + K_L C} \tag{2}$$

where k_r represents the rate constant for surface photocatalysis. At extremely low reactant concentrations, the denominator in the above equation approaches zero, so Eq. (3) can be simplified as;

$$\ln\frac{C}{C_0} = -k_r K_L t = -k_{obs}t \tag{3}$$

where k_{obs} represents the observed rate constant for photodegradation, C is the concentration of Ph after degradation, C_0 is the initial concentration of Ph, and t represents the irradiation time. The percentage of Ph degradation was calculated following Eq. (4);

$$\% \text{ Ph degradation} = \frac{C_i - C_f}{C_i} \times 100\% \tag{4}$$

where C_i and C_f are the initial and the final concentration of Ph, respectively [33].

■ RESULTS AND DISCUSSION

Functional group identification in Cu-N-ZT composites was done by FTIR characterization. Fig. 1 shows the FTIR spectra of Cu-N-ZT-500 with different Cu concentrations, using ZrO$_2$ and N-ZT-500 as references. A broad absorption band between 500–600 cm^{-1} is attributed to the stretching vibrations of Ti−O
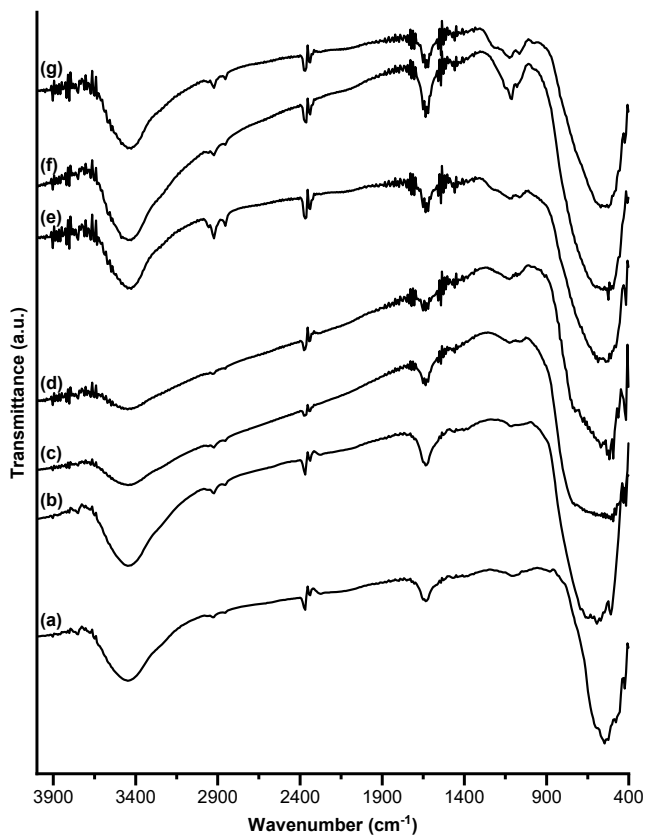
Fig 1. FTIR spectra of (a) ZrO$_2$, (b) N-ZT-500, (c) 1Cu, (d) 3Cu, (e) 5Cu, (f) 7Cu, and (g) 9Cu-N-ZT-500

and Cu−O [34]. The peaks at wavenumbers 512 and 1,635 cm^{-1} confirm the presence of ZrO$_2$, as both are designated to the Zr−O and Zr−OH vibrational bands, respectively [35]. The absorption band at approximately 1,120 cm^{-1} increases as the percentage of Cu dopant increases up to 7%. This may indicate the presence of Cu−O−Zr or Cu−O−Ti bonds or both. In N-ZT-500, the peak intensity at 1,600 cm^{-1} is stronger and sharper than in ZrO$_2$, suggesting the presence of N dopant in the crystal lattice [36]. The O−H stretching vibration of H$_2$O is recognized as the absorption band at 3,400 cm^{-1} in all samples [37]. The composite is indicated to contain water molecules that were adsorbed during the synthesis process.

FTIR spectra of 5Cu-N-ZT calcined at various temperatures are shown in Fig. 2. A weak absorption peak of Zr−O at 500–600 cm^{-1} in 5Cu-N-ZT-700 and 5Cu-N-ZT-900 indicates the anatase-to-rutile transformation [38]. The decrease in O−H absorptions at 3,300–3,400 and 1,600 cm^{-1} as the calcination temperature increases is due

to the removal of water molecules [39]. Additionally, the Ti−O−Cu vibration at 1,120 cm^{-1} decreases in 5Cu-N-ZT-700 and disappears at 5Cu-N-ZT-900, indicating the sintering of metal dopant caused by the high calcination temperature [40].

Diffraction patterns of 5Cu-N-ZT with various calcination temperatures are shown in Fig. 3 alongside ZrO$_2$, TiO$_2$, and N-ZT-500 as reference. The average
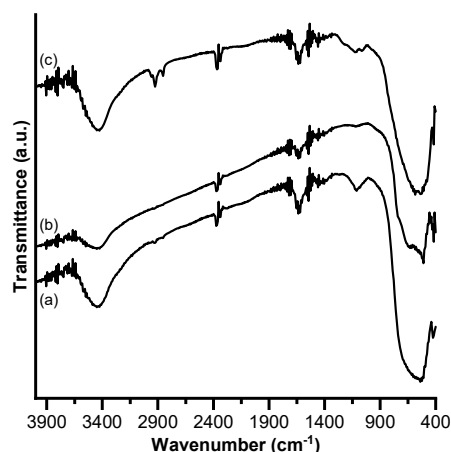

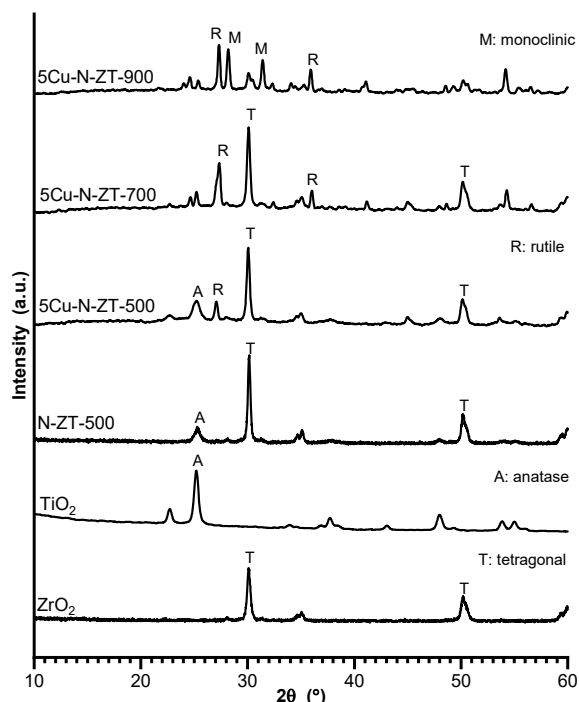**Fig 2.** FTIR spectra of 5Cu-N-ZT (a)-500, (b)-700, and (c)-900

Fig 3. XRD patterns of 5Cu-N-ZT composite calcined at various temperatures

crystallite sizes of different 5Cu-N-ZT composites are given in Table 1. The diffraction pattern of ZrO_2 and TiO_2 calcined at 500 °C shows the presence of tetragonal and anatase phases. Based on ICDD (01-081-1545) as reference peaks of ZrO_2 (tetragonal), characteristic of the tetragonal phase appeared at $2\theta = 30°$ (d_{101}) and $50°$ (d_{112}). The characteristic peaks of TiO_2 anatase (ICDD: 01-078-2486) appeared at $2\theta = 25°$ (d_{101}) and $48°$ (d_{200}). The peaks of the anatase phase broaden significantly after Cu and N codoping. Codoping with Cu and N would produce smaller anatase crystals because it was able to inhibit the growth of TiO_2 crystals [41]. The diffraction pattern of 5Cu-N-ZT-500 has a characteristic low-intensity anatase peak at $25°$ (d_{101}). Crystallization from amorphous to anatase is inhibited by the presence of copper and nitrogen dopants [42]. The presence of Zr^{4+} in the TiO_2 system also inhibits the transformation of anatase to rutile [22]. 5Cu-N-ZT-700 shows rutile characteristics at $2\theta = 27.3°$ (d_{110}) and $36°$ (d_{101}), while the anatase peak decreases at $2\theta = 25°$ (d_{101}) and the rutile peak increases at $2\theta = 27.3°$. The rutile (ICDD: 01-077-0442) diffraction pattern intensifies at $2\theta = 27.3°$ (d_{110}) and $36°$ (d_{101}) when the calcination temperature is increased to 900 °C. The diffraction pattern of 5Cu-N-ZT-900 indicates typical rutile and anatase patterns at angles of $2\theta = 27°$ (d_{110}), $36°$ (d_{101}), $41°$ (d_{111}), $54°$ (d_{211}), and $2\theta = 25°$ (d_{101}), $48°$ (d_{200}) respectively. This is because ZrO_2 and N dopants prevent the transformation of anatase to rutile [43]. The tetragonal phase also transforms into a monoclinic (ICDD: 01-078-0047) phase after calcination at 900 °C, as shown by the appearance of diffraction peaks at $2\theta = 28°$ (d_{-111}) and $31°$ (d_{111}).

The average crystallite sizes of both 5Cu-N-ZT-700 and 5Cu-N-ZT-900 composites were calculated to observe any changes at different temperatures of calcination. Based on Table 1, the average crystallite size of the 700 and 900 composites in the anatase phase decreased by 59 and 41 nm, respectively. The reduction in the anatase size results from the formation of a more rutile phase than anatase, so the reduction in the anatase phase corresponds to the increase in the size of the rutile phase [44]. This is also attributed to the higher calcination temperature, which enhances better anatase crystal growth [45]. On the

Table 1. Average crystallite size of 5Cu-N-ZT calcined at various temperatures

Material	Crystal phase	L (nm)
ZrO_2 500 °C	Tetragonal	45
TiO_2 500 °C	Anatase	18
N-ZT-500	Tetragonal	45
	Anatase	15
5Cu-N-ZT-500	Tetragonal	19
	Anatase	22
5Cu-N-ZT-700	Tetragonal	22
	Anatase	59
	Rutile	81
5Cu-N-ZT-900	Monoclinic	57
	Anatase	41
	Rutile	82

other hand, the crystallite size of the tetragonal phase decreased from 45 to 19 nm in the 5Cu-N-ZT-500 composite compared to the reference ZrO_2 and N-ZT-500. The decrease in crystal size due to the addition of 5% Cu dopant causes oxygen defects so that the crystal lattice shrinks [16]. In addition, dopants can also inhibit the growth of metastable tetragonal crystals [46]. The monoclinic phase is observed at a calcination temperature of 900, with a crystal size of 57 nm, which is the largest. There is a chance for moisture to be present in the tetragonal crystal phase (5Cu-N-ZT-500) that facilitates the growth of the low-temperature tetragonal phase [47]. Hence, with the progress in calcination temperatures, the tetragonal phase of 5Cu-N-ZT-900 composite transforms into a monoclinic phase, accompanied by a decrease in water content in the crystal lattice structure [48].

SEM images of 5Cu-N-ZT-500 composite and ZrO_2 reference are presented in Fig. 4. The SEM images were taken at a magnification of 10,000. The particle size distribution of 5Cu-N-ZT-500, which is smaller than that of ZrO_2, causes the morphology of 5Cu-N-ZT-500 to appear more homogeneous compared to the reference ZrO_2 [49]. Table 2 summarizes the elemental composition of the surface of ZrO_2 and 5Cu-N-ZT-500 based on the SEM image in Fig. 4. Zr mass percentage is similar to Ti, and Zr in the composite acts as a carrier to support the stability of the material [50]. The low Cu content detected
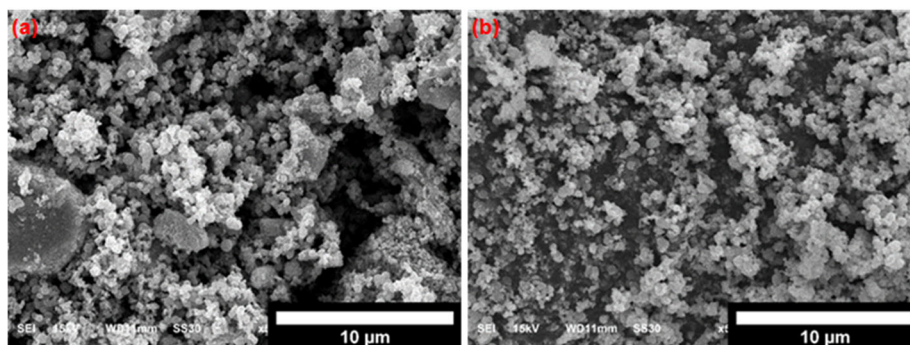
Fig 4. SEM photographs of (a) ZrO_2 and (b) 5Cu-N-ZT-500

Table 2. EDX analysis of ZrO_2 and 5-Cu-N-ZT-500

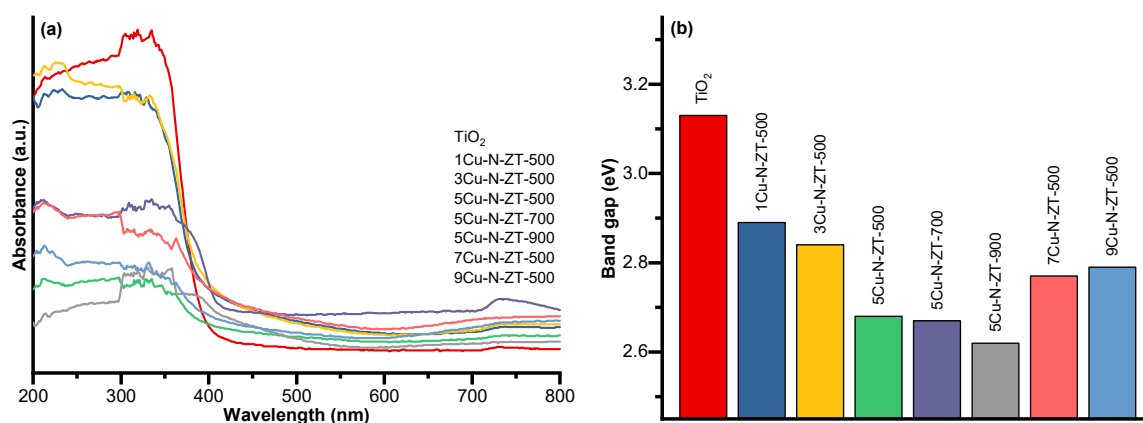| Material	% Mass					
	Zr	O	Ti	N	Cu	Total
ZrO_2	50.31	49.69	-	-	-	100
5Cu-N-ZT-500	29.69	38.83	25.43	0.60	5.44	100

Fig 5. (a) UV-vis absorption spectra and (b) band gap of various Cu-N-ZT composites

is due to the heterogeneous distribution of Cu dopants on the surface of $ZrTiO_4$.

Fig. 5(a) displays the UV-vis spectra of Cu-N-ZT with various Cu concentrations and calcination temperatures. The inflection point (absorption edge) of all codoped composites existing above 400 nm is due to the heterojunction between the valence and conduction bands of ZrO_2 with TiO_2 [51]. The band gap (E_g) of the synthesized composite is shown in Fig. 5(b). Codoping of Cu and N into $ZrTiO_4$ composite shifts the E_g from 3.13 to 2.68 eV. The E_g is reduced up to 5% Cu doping, then is increased again as copper concentration increases as well. Cu doping with excess concentration can cause sintering, which forms aggregates that are not evenly distributed [24].

The E_g of $ZrTiO_4$ is slightly smaller due to the broad E_g of ZrO_2 mixing with the relatively narrow E_g of TiO_2 until the equilibrium is reached. The insertion of N and Cu into the $ZrTiO_4$ system can shift the absorption edge towards the visible light region until saturation is reached [52]. If the amount of dopants has reached saturation point, their effect is reduced. The addition of Cu and N dopants successfully shifts the absorption band to longer wavelengths, from 333.97 to 473.27 nm within the visible light region. In Fig. 5(b), it shows decreasing E_g of 5Cu-N-ZT-500, 5Cu-N-ZT-700 and 5Cu-N-ZT-900. This is caused by an increase in the calcination temperature that favors the transformation of anatase to rutile, in which the rutile phase has a narrower E_g than the anatase phase [53].

The photocatalytic activity of Cu-N-ZT was evaluated by degrading Ph in the dark (reaction time before 0 min) and under visible light irradiation using a LIFE MAX 30W/765 PHILIPS TLD lamp. Fig. 6(a) shows the percentage of degraded Ph. In the absence of a light source to generate •OH radicals, the percentage was very small (less than 5%).

Under visible light conditions, the degradation results increase because visible light has a large intensity and wavelength of 765 nm which can generate •OH radicals from water molecules [54]. Under high energy irradiation, the photocatalyst produces strong oxidizing agents in the form of h+, which in turn generate •OH radicals. These radicals are responsible for the degradation of Ph into simpler compounds [55]. According to Fig. 6(a), there was a significant increase in the percentage of degradation during the 0 to 75 min interval, while the increase in degradation during the 75 to 120 min interval was not significant. To compare the activity, plots were provided for an irradiation time of 0 to 75 min, as the highest photoactivity was observed during this time interval. The linear plot shows that the reaction conforms to pseudo-first-order kinetics [32]. Fig. 6(b) presents the observed rate constant of the synthesized composites.

Based on Fig. 6(a) the percentage of Ph degrades increases as the Cu dopant increases to 5%, reaching up to 91% of 10 mg L^{-1} Ph solution after 75 min irradiation. The composite of Cu-N-ZrTiO$_4$, containing 5% Cu and calcined at 500 °C, exhibits the maximum photocatalytic activity, whereas the composite with 1% Cu and calcined at the same temperature displays the minimum photocatalytic activity. The photocatalytic activity of the composite reduces with the rise in the Cu amount beyond 5%, owing to the decline in the doping effect caused by Cu saturation [56]. Photodegradation activity decreases at 5Cu-N-ZT-700 and 5Cu-N-ZT-900 due to the existence of rutile. High calcination temperatures lead to an anatase to rutile phase transformation in TiO$_2$. The formation of the rutile phase with sharp intensities at 2θ = 27° (d$_{110}$), 36° (d$_{101}$), 41° (d$_{111}$), and 54° (d$_{211}$), is demonstrated through the XRD characterization of the 5Cu-N-ZT-700 and 5Cu-N-ZT-900 materials. Rutile is the polymorph that has the narrowest band gap, but it mostly exhibits photocatalytic activity that is lower than that of anatase [14]. In line with the percentage degradation in Fig. 6(a), the k$_{obs}$ value also experienced the highest increase of 0.0362 min^{-1} in the 5Cu-N-ZT-500 composite. The k$_{obs}$ values of both composites decreased, with 5Cu-N-ZT-700 and 5Cu-N-ZT-900 composites experiencing a reduction of 0.0262 and 0.0319 min^{-1}, respectively. This decrease can be attributed to a higher composition of rutile in both composites compared to anatase.

All Cu-N-ZT composites exhibit higher photocatalytic activity than the reference N-ZT-500. Co-doping Cu enhances the photocatalytic activity of N-ZT-500, with 5Cu-N-ZT-500 delivering the highest activity. The results indicate that the coupling of ZrO$_2$-TiO$_2$ and the co-doping of Cu and N effectively improve the photocatalytic activity.
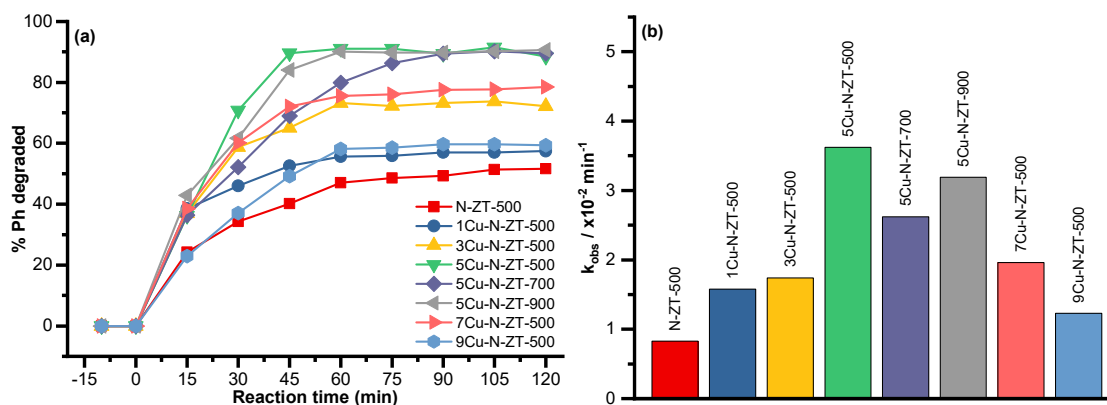

Fig 6. (a) Photodegradation of Ph over irradiation time and (b) observed rate constant k$_{obs}$ of Ph photodegradation by various Cu-N-ZT composite

■ **CONCLUSION**

The Cu-N-codoped ZrTiO$_4$ photocatalyst composite was prepared through the sol-gel process. The FTIR analysis showed an absorption band at 1,200 cm^{-1}, which corresponds to the Ti–O–Cu vibration. The absorption band gets sharper at 7% Cu concentration. The XRD patterns of Cu-N-codoped ZrTiO$_4$ reveal that codoping with Cu and N produces smaller anatase crystallite size due to the growth inhibition of TiO$_2$ crystals. The addition of 5% Cu and N dopants results in the lowest E$_g$ of 2.62 eV, making it more suitable for visible light. The Cu-N-ZT-500 photocatalyst degraded 10 mg L^{-1} Ph solution up to 91% after 75 min of irradiation time. The photocatalytic activity of ZrTiO$_4$ can be enhanced by codoping with Cu and N, making it a potential photocatalyst for the photodegradation of phenol in an aqueous solution under visible light irradiation. However, further studies are required to determine the stability of the composite.

■ **CONFLICT OF INTEREST**

All authors certify that they have no affiliations with or involvement in any organization or entity with any financial interest or non-financial interest in the subject matter or materials discussed in this manuscript.

■ **AUTHOR CONTRIBUTIONS**

Wanda Putra Fauzi served as researcher, data collector, and first writer and conducted revisions. Rian Kurniawan, Sri Sudiono, and Niko Prasetyo, as co-authors, checked revision results, and provided suggestions for improvements in the written report. Akhmad Syoufian served as the corresponding author and research supervisor, checked revision results, provided suggestions for improvements, and conducted final assessments of the data and the written report.

■ **REFERENCES**

[1] Crini, G., and Lichtfouse, E., 2019, Advantages and disadvantages of techniques used for wastewater treatment, *Environ. Chem. Lett.*, 17 (1), 145–155.

[2] Gadipelly, C., Pérez-González, A., Yadav, G.D., Ortiz, I., Ibáñez, R., Rathod, V.K., and Marathe, K.V., 2014, Pharmaceutical industry wastewater: Review of the technologies for water treatment and reuse, *Ind. Eng. Chem. Res.*, 53 (29), 11571–11592.

[3] Naguib, D.M., and Badawy, N.M., 2020, Phenol removal from wastewater using waste products, *J. Environ. Chem. Eng.*, 8 (1), 103592.

[4] Villegas, L.G.C., Mashhadi, N., Chen, M., Mukherjee, D., Taylor, K.E., and Biswas, N., 2016, A short review of techniques for phenol removal from wastewater, *Curr. Pollut. Rep.*, 2 (3), 157–167.

[5] Dehmani, Y., Mobarak, M., Oukhrib, R., Dehbi, A., Mohsine, A., Lamhasni, T., Tahri, Y., Ahlafi, H., Abouarnadasse, S., Lima, E.C., and Badawi, M., 2023, Adsorption of phenol by a Moroccan clay/hematite composite: Experimental studies and statistical physical modeling, *J. Mol. Liq.*, 386, 122508.

[6] Khleifat, K., Magharbeh, M., Alqaraleh, M., Al-Sarayrah, M., Alfarrayeh, I., Al Qaisi, Y., Alsarayreh, A., and Al-kafaween, M.A., 2022, Biodegradation modeling of phenol using *Curtobacterium flaccumfaciens* as plant-growth-promoting bacteria, *Heliyon*, 8 (9), e10490.

[7] Sacco, O., Vaiano, V., Daniel, C., Navarra, W., and Venditto, V., 2018, Removal of phenol in aqueous media by N-doped TiO$_2$ based photocatalytic aerogels, *Mater. Sci. Semicond. Process.*, 80, 104–110.

[8] Bharali, D., Saikia, S., Devi, R., Choudary, B.M., Gour, N.K., and Deka, R.C., 2023, Photocatalytic degradation of phenol and its derivatives over ZnFe layered double hydroxide, *J. Photochem. Photobiol., A*, 438, 114509.

[9] Qi, K., Wang, Z., Xie, X., and Wang, Z., 2023, Photocatalytic performance of pyrochar and hydrochar in heterojunction photocatalyst for organic pollutants degradation: Activity comparison and mechanism insight, *Chem. Eng. J.*, 467, 143424.

[10] Ur Rehman, G., Tahir, M., Goh, P.S., Ismail, A.F., Hafeez, A., and Khan, I.U., 2021, Enhancing the photodegradation of phenol using Fe$_3$O$_4$/SiO$_2$ binary nanocomposite mediated by silane agent, *J. Phys. Chem. Solids*, 153, 110022.

[11] Viet, N.M., Mai Huong, N.T., and Thu Hoai, P.T., 2023, Enhanced photocatalytic decomposition of phenol in wastewater by using La–TiO$_2$ nanocomposite, *Chemosphere*, 313, 137605.

[12] Quirk, J.A., Lazarov, V.K., and McKenna, K.P., 2020, First-principles modeling of oxygen-deficient anatase TiO$_2$ nanoparticles, *J. Phys. Chem. C*, 124 (43), 23637–23647.

[13] Hu, Y., Tsai, H.L., and Huang, C.L., 2003, Effect of brookite phase on the anatase–rutile transition in titania nanoparticles, *J. Eur. Ceram. Soc.*, 23 (5), 691–696.

[14] Zhang, J., Zhou, P., Liu, J., and Yu, J., 2014, New understanding of the difference of photocatalytic activity among anatase, rutile and brookite TiO$_2$, *Phys. Chem. Chem. Phys.*, 16 (38), 20382–20386.

[15] Reddy, C.V., Babu, B., Reddy, I.N., and Shim, J., 2018, Synthesis and characterization of pure tetragonal ZrO$_2$ nanoparticles with enhanced photocatalytic activity, *Ceram. Int.*, 44 (6), 6940–6948.

[16] Arjun, A., Dharr, A., Raguram, T., and Rajni, K.S., 2020, Study of copper doped zirconium dioxide nanoparticles synthesized via sol–gel technique for photocatalytic applications, *J. Inorg. Organomet. Polym. Mater.*, 30 (12), 4989–4998.

[17] Bandara, W.R.L.N., de Silva, R.M., de Silva, K.M.N., Dahanayake, D., Gunasekara, S., and Thanabalasingam, K., 2017, Is nano ZrO$_2$ a better photocatalyst than nano TiO$_2$ for degradation of plastics?, *RSC Adv.*, 7 (73), 46155–46163.

[18] Verma, S., Rani, S., Kumar, S., and Khan, M.A.M., 2018, Rietveld refinement, micro-structural, optical and thermal parameters of zirconium titanate composites, *Ceram. Int.*, 44 (2), 1653–1661.

[19] Kim, J.Y., Kim, C.S., Chang, H.K., and Kim, T.O., 2011, Synthesis and characterization of N-doped TiO$_2$/ZrO$_2$ visible light photocatalysts, *Adv. Powder Technol.*, 22 (3), 443–448.

[20] Bashirom, N., Tan, W.K., Kawamura, G., Matsuda, A., and Lockman, Z., 2022, Formation of self-organized ZrO$_2$–TiO$_2$ and ZrTiO$_4$–TiO$_2$ nanotube arrays by anodization of Ti–40Zr foil for Cr(VI) removal, *J. Mater. Res. Technol.*, 19, 2991–3003.

[21] Kurniawan, R., Sudiono, S., Trisunaryanti, W., and Syoufian, A., 2019, Synthesis of iron-doped zirconium titanate as a potential visible-light responsive photocatalyst, *Indones. J. Chem.*, 19 (2), 454–460.

[22] Muslim, M.I., Kurniawan, R., Pradipta, M.F., Trisunaryanti, W., and Syoufian, A., 2021, The effects of manganese dopant content and calcination temperature on properties of titania-zirconia composite, *Indones. J. Chem.*, 21 (4), 882–890.

[23] Alifi, A., Kurniawan, R., and Syoufian, A., 2020, Zinc-doped titania embedded on the surface of zirconia: A potential visible-responsive photocatalyst material, *Indones. J. Chem.*, 20 (6), 1374–1381.

[24] Hayati, R., Kurniawan, R., Prasetyo, N., Sudiono, S., and Syoufian, A., 2022, Codoping effect of nitrogen (N) to iron (Fe) doped zirconium titanate (ZrTiO$_4$) composite toward its visible light responsiveness as photocatalysts, *Indones. J. Chem.*, 22 (3), 692–702.

[25] Wang, J., Zhao, Y.F., Wang, T., Li, H., and Li, C., 2015, Photonic, and photocatalytic behavior of TiO$_2$ mediated by Fe, CO, Ni, N doping and co-doping, *Phys. B*, 478, 6–11.

[26] Lin, H., and Shih, C., 2016, Efficient one-pot microwave-assisted hydrothermal synthesis of M (M=Cr, Ni, Cu, Nb) and nitrogen co-doped TiO$_2$ for hydrogen production by photocatalytic water splitting, *J. Mol. Catal. A: Chem.*, 411, 128–137.

[27] Doong, R., and Liao, C.Y., 2017, Enhanced visible-light-responsive photodegradation of bisphenol A by Cu, N-codoped titanate nanotubes prepared by microwave-assisted hydrothermal method, *J. Hazard. Mater.*, 322, 254–262.

[28] Fan, X., Lin, L., and Messersmith, P.B., 2006, Surface-initiated polymerization from TiO$_2$ nanoparticle surfaces through a biomimetic initiator: A new route toward polymer–matrix

nanocomposites, *Compos. Sci. Technol.*, 66 (9), 1198–1204.

[29] Rahmawati, L., Kurniawan, R., Prasetyo, N., Sudiono, S., and Syoufian, A., 2023, Copper-and-nitrogen-codoped zirconium titanate (Cu-N-ZrTiO$_4$) as a photocatalyst for photo-degradation of methylene blue under visible-light irradiation, *Indones. J. Chem.*, 23 (2), 416–424.

[30] Albornoz Marin, S.L., de Oliveira, S.C., and Peralta-Zamora, P., 2022, Photocatalytic degradation of phenol by core–shell Cu@TiO$_2$ nanostructures under visible radiation, *J. Photochem. Photobiol., A*, 433, 114129.

[31] Kambur, A., Pozan, G.S., and Boz, I., 2012, Preparation, characterization and photocatalytic activity of TiO$_2$–ZrO$_2$ binary oxide nanoparticles, *Appl. Catal., B*, 115-116, 149–158.

[32] Fu, C.C., Juang, R.S., Huq, M.M., and Hsieh, C.T., 2016, Enhanced adsorption and photodegradation of phenol in aqueous suspensions of titania/graphene oxide composite catalysts, *J. Taiwan Inst. Chem. Eng.*, 67, 338–345.

[33] Fazal, T., Razzaq, A., Javed, F., Hafeez, A., Rashid, N., Amjad, U.S., Ur Rehman, M.S., Faisal, A., and Rehman, F., 2020, Integrating adsorption and photocatalysis: A cost effective strategy for textile wastewater treatment using hybrid biochar-TiO$_2$ composite, *J. Hazard. Mater.*, 390, 121623.

[34] Arora, P., Fermah, A., Rajput, J.K., Singh, H., and Badhan, J., 2017, Efficient solar light-driven degradation of Congo red with novel Cu-loaded Fe$_3$O$_4$@TiO$_2$ nanoparticles, *Environ. Sci. Pollut. Res.*, 24 (24), 19546–19560.

[35] Zhu, X., Li, B., Yang, J., Li, Y., Zhao, W., Shi, J., and Gu, J., 2015, Effective adsorption and enhanced removal of organophosphorus pesticides from aqueous solution by Zr-based MOFs of UiO-67, *ACS Appl. Mater. Interfaces*, 7 (1), 223–231.

[36] Reda, S.M., Khairy, M., and Mousa, M.A., 2020, Photocatalytic activity of nitrogen and copper doped TiO$_2$ nanoparticles prepared by microwave-assisted sol-gel process, *Arabian J. Chem.*, 13 (1), 86–95.

[37] Dlapa, P., Bodí, M.B., Mataix-Solera, J., Cerdà, A., and Doerr, S.H., 2013, FT-IR spectroscopy reveals that ash water repellency is highly dependent on ash chemical composition, *Catena*, 108, 35–43.

[38] Farhadian Azizi, K., and Bagheri-Mohagheghi, M.M., 2013, Transition from anatase to rutile phase in titanium dioxide (TiO$_2$) nanoparticles synthesized by complexing sol–gel process: Effect of kind of complexing agent and calcinating temperature, *J. Sol-Gel Sci. Technol.*, 65 (3), 329–335.

[39] Sulaikhah, E.F., Kurniawan, R., Pradipta, M.F., Trisunaryanti, W., and Syoufian, A., 2020, Cobalt doping on zirconium titanate as a potential photocatalyst with visible-light-response, *Indones. J. Chem.*, 20 (4), 911–918.

[40] Shao, G.N., Imran, S.M., Jeon, S.J., Engole, M., Abbas, N., Salman Haider, M., Kang, S.J., and Kim, H.T., 2014, Sol–gel synthesis of photoactive zirconia–titania from metal salts and investigation of their photocatalytic properties in the photodegradation of methylene blue, *Powder Technol.*, 258, 99–109.

[41] Wang, S., Yang, X.J., Jiang, Q., and Lian, J.S., 2014, Enhanced optical absorption and photocatalytic activity of Cu/N-codoped TiO$_2$ nanocrystals, *Mater. Sci. Semicond. Process.*, 24, 247–253.

[42] Singha, K., Ghosh, S.C., and Panda, A.B., 2021, Visible light-driven efficient synthesis of amides from alcohols using Cu−N−TiO$_2$ heterogeneous photocatalyst, *Eur. J. Org. Chem.*, 2021 (4), 657–662.

[43] Suwannaruang, T., Hildebrand, J.P., Taffa, D.H., Wark, M., Kamonsuangkasem, K., Chirawatkul, P., and Wantala, K., 2020, Visible light-induced degradation of antibiotic ciprofloxacin over Fe−N−TiO$_2$ mesoporous photocatalyst with anatase/rutile/brookite nanocrystal mixture, *J. Photochem. Photobiol., A*, 391, 112371.

[44] Velardi, L., Scrimieri, L., Serra, A., Manno, D., and Calcagnile, L., 2020, Effect of temperature on the physical, optical and photocatalytic properties of TiO$_2$ nanoparticles, *SN. Appl. Sci.*, 2 (4), 707.

[45] Zhang, Q., and Li, C., 2020, High temperature stable anatase phase titanium dioxide films synthesized by mist chemical vapor deposition, *Nanomaterials*, 10 (5), 911.

[46] Kogler, M., Köck, E.M., Vanicek, S., Schmidmair, D., Götsch, T., Stöger-Pollach, M., Hejny, C., Klötzer, B., and Penner, S., 2014, Enhanced kinetic stability of pure and Y-doped tetragonal ZrO_2, *Inorg. Chem.*, 53 (24), 13247–13257.

[47] Xie, S., Iglesia, E., and Bell, A.T., 2000, Water-assisted tetragonal-to-monoclinic phase transformation of ZrO_2 at low temperatures, *Chem. Mater.*, 12 (8), 2442–2447.

[48] Kim, H.T., Han, J.S., Yang, J.H., Lee, J.B., and Kim, S.H., 2009, The effect of low temperature aging on the mechanical property & phase stability of Y-TZP ceramics, *J. Adv. Prosthodont.*, 1 (3), 113–117.

[49] Sarkar, N., Park, J.G., Mazumder, S., Aneziris, C.G., and Kim, I.J., 2015, Processing of particle stabilized Al_2TiO_5–$ZrTiO_4$ foam to porous ceramics, *J. Eur. Ceram. Soc.*, 35 (14), 3969–3976.

[50] Xia, Y., Mou, J., Deng, G., Wan, S., Tieu, K., Zhu, H., and Xue, Q., 2020, Sintered ZrO_2–TiO_2 ceramic composite and its mechanical appraisal, *Ceram. Int.*, 46 (1), 775–785.

[51] Chang, S.M., and Doong, R., 2006, Characterization of Zr-doped TiO_2 nanocrystals prepared by a nonhydrolytic sol-gel method at high temperatures, *J. Phys. Chem. B*, 110 (42), 20808–20814.

[52] Colón, G., Maicu, M., Hidalgo, M.C., and Navío, J.A., 2006, Cu-doped TiO_2 systems with improved photocatalytic activity, *Appl. Catal., B*, 67 (1-2), 41–51.

[53] Tryba, B., Orlikowski, J., Wróbel, R.J., Przepiórski, J., and Morawski, A.W., 2015, Preparation and characterization of rutile-type TiO_2 doped with Cu, *J. Mater. Eng. Perform.*, 24 (3), 1243–1252.

[54] Tzompantzi, F., Castillo-Rodríguez, J.C., Tzompantzi-Flores, C., Pérez-Hernández, R., Gómez, R., Santolalla-Vargas, C.E., Che-Galicia, G., and Ramos-Ramírez, E., 2022, Addition of SnO_2 over an oxygen deficient zirconium oxide (ZrxOy) and its catalytic evaluation for the photodegradation of phenol in water, *Catal. Today*, 394–396, 376–389.

[55] Feng, C., Chen, Z., Jing, J., and Hou, J., 2020, The photocatalytic phenol degradation mechanism of Ag-modified ZnO nanorods, *J. Mater. Chem. C*, 8 (9), 3000–3009.

[56] Bhattacharyya, K., Mane, G.P., Rane, V., Tripathi, A.K., and Tyagi, A.K., 2021, Selective CO_2 photoreduction with Cu-doped TiO_2 photocatalyst: Delineating the crucial role of Cu-oxidation state and oxygen vacancies, *J. Phys. Chem. C*, 125 (3), 1793–1810.